

A thin, large area microstrip gas chamber with strip and pad readout

F. Angelini, R. Bellazzini, A. Brez, T. Lomtadze, M.M. Massai, R. Raffo, G. Spandre
and M.A. Spezziga

INFN-Pisa and University of Pisa, Via Livornese 582, I-56010 S. Piero a Grado, Pisa, Italy

Received 2 April 1993 and in revised form 28 June 1993

The design, construction and test of a thin (200 μm overall substrate thickness), large area (10 cm \times 10 cm) microstrip gas chamber (MSGC) with both strip and pad readout is described. The device is built on a 6 in. silicon wafer. The characteristics of this detector make it suitable as a building block of a tracking system at LHC/SSC

1. Introduction

Since its introduction [1,2], the microstrip gas chamber has been considered one of the most promising detectors for the instrumentation of the next generation of experiments at high luminosity machines [3,4]. This is due to very good detector performance, now very close to those of a solid state microstrip detector, as well as to its simplicity, low-cost and radiation resistance (intrinsic to a flushed detector with internal gas gain). Because of these features, this detector was quite early successfully used to track particles in two fixed target experiments at CERN, NA12 [5] and RD22 [6], clearly showing that it is already a useful instrument for present day physics.

Moving from fixed target medium scale experiments, having at most thousands of channels, to huge collider experiments at LHC/SSC with millions of readout channels is, obviously, a large step forward. Nevertheless, almost all the experiments which have been proposed for both LHC and SSC include the use of MSGCs in the tracking system [7,8]. Common to all these proposals is the need for MSGCs with:

- i) the largest possible area (typically 100 cm²) compatible with low occupancy to reduce the number of channels when covering large volumes;
- ii) thin substrates to reduce multiple scattering and photon conversion;
- iii) enough radiation resistance to survive in the extremely severe environmental conditions;
- iv) 2-D readout to manage the high particle multiplicity, especially in the forward region.

This paper reports on the design, construction and test of a MSGC built on a thin (200 μm) 6 in. silicon wafer, fulfilling all these requirements.

2. The detector

2.1. The detector internal structure

The operation of a microstrip gas chamber built on a silicon substrate has been already demonstrated [9–11]. What is new in the approach presented in this paper is the large active area, the thin substrate and the 2-D capability. Fig. 1 shows a cross-section of the detector's internal structure.

Moving from bottom to top we observe:

i) The 10 cm \times 10 cm low resistivity silicon substrate (200 μm thick), which acts only as a mechanical support, onto which a 2 μm thick SiO₂ layer was thermally grown to provide the necessary insulation from the overlying first metal layer. The silicon substrate was made so thin by back-grinding a 6 in. silicon wafer, whose original thickness was 600 μm , at the end of the detector fabrication procedure. This is a standard technique in the microelectronics industry.

ii) The first aluminum film (Metal 1, 0.8 μm thick) deposited on the underlying thermal oxide layer. The Al film was then patterned by standard photolithography and dry etching techniques to realise the readout structure of the back electrode.

iii) The 2 μm thick SiO₂ layer (Intermetal Oxide), obtained by plasma enhanced chemical vapour deposition (PECVD). It represents the effective substrate thickness and it has been implanted with a dose of 4×10^{16} boron ions/cm² to control charging effects.

iv) The second aluminum film (Metal 2, 2 μm thick) deposited onto the chemical oxide layer and on which 512 anode-cathode amplifying structures were engraved with a plasma etching technique

v) The gas gap (3 mm) which acts as active medium.

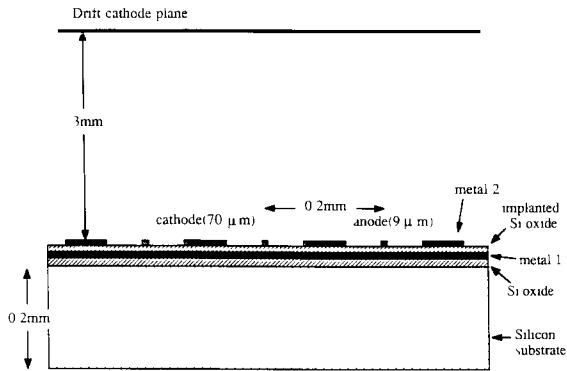


Fig. 1. A cross section of the detector internal structure.

vi) The drift electrode that defines the region of collection of the primary charge.

The present detector is built on a 6-in. silicon wafer but 8-in. technology is also available. Any substrate material compatible with the silicon processing lines can be used as well (silicon, sapphire, high quality glass, etc.).

A photograph of the detector still on the silicon wafer before cutting is shown in fig. 2. The detector was then cut with $20\ \mu\text{m}$ precision using a laser saw. A dead space of only $200\ \mu\text{m}$ was allowed along the four sides. Two detectors can be mounted head-on with the anode strips readout individually on the opposite sides, thus providing a $20\ \text{cm} \times 10\ \text{cm}$ module having negligible dead space. This kind of module is close to ideal, in terms of granularity, occupancy, number of channels and yield for the large tracking systems planned for LHC/SSC [7,8].

2.2. The electrostatic field

To understand the operation of this device we have studied in detail the electric field configuration using a commercial electrostatic modeler (ELECTRO, IES, Manitoba, Canada) which includes also dielectrics and resistive materials. Fig. 3a shows the field and the equipotential lines for a non-implanted thin oxide layer with $10^{17}\ \Omega\ \text{cm}$ resistivity which is typical for a good silicon oxide. The most striking feature is the large

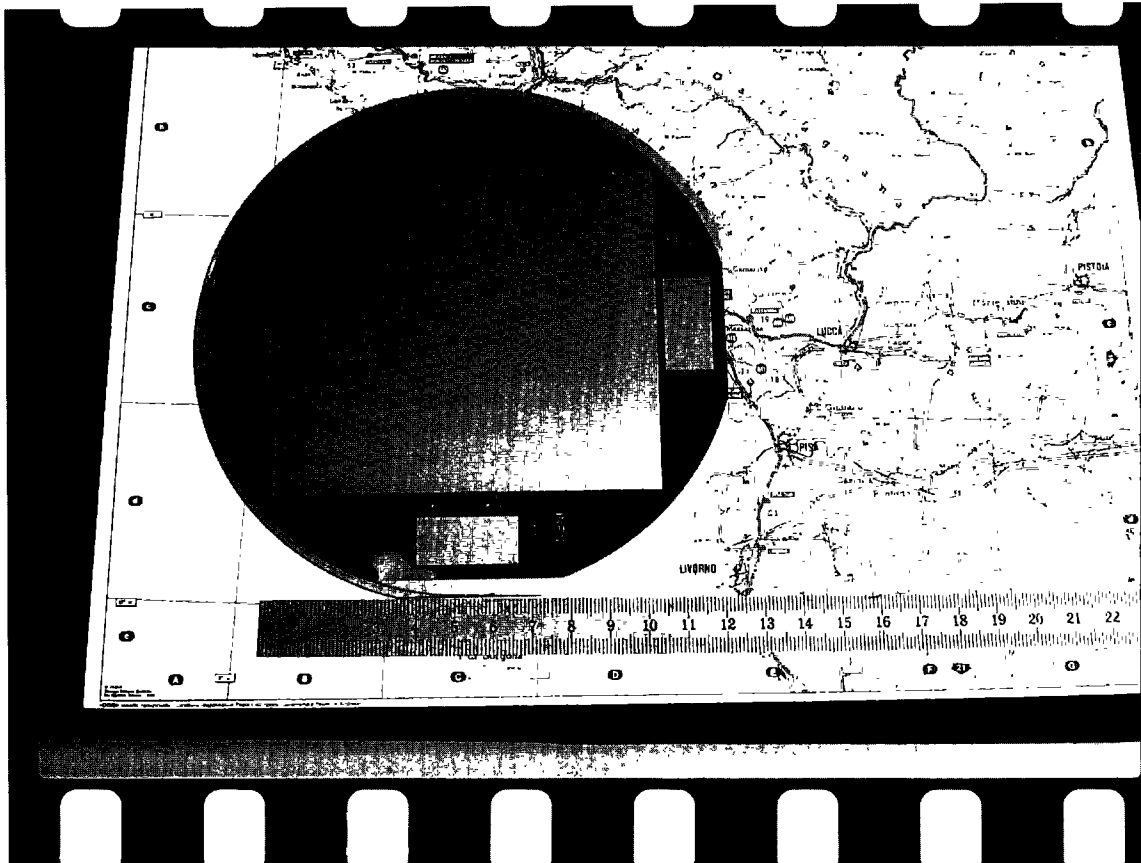


Fig. 2. A photograph of the detector still on the silicon wafer.

number of field lines entering the substrate and the very steep voltage gradients. In such a configuration the detector could hardly work in a stable way because of the very fast charging-up of the substrate by the positive ions. The field map is considerably changed (see fig. 3b) when a $0.2 \mu\text{m}$ thick oxide layer with a bulk resistivity of $10^{12}\text{--}10^{13} \Omega \text{ cm}$ is added just below Metal 2. The reduction of resistivity of this very thin layer is due to the implantation process. Now the voltage gradients are much weaker and there are no longer field lines entering the substrate in the proximity of the anode but only field lines leaving it. This dramatic modification of the field is due to the accumulation of free charges at the interface between materials with different resistivities. The new field map is much closer to the standard map for a thick implanted substrate (see fig. 4). In contrast with our previous naive expectations [12] the back plane, even if it is very close to the anode strip, does not play a dominant role in shaping the field because its presence is largely shielded by the implanted layer. Fig. 5 shows the equipotential lines for the non-implanted and the im-

planted structure, clearly showing the field smoothing effect of the implantation process, as already suggested in ref. [13]. The implanted layer acts as a thin, rectangular resistor inside which the electric field is almost uniform and parallel to its external surfaces. This shape of the field is due to the large resistivity gradient (5 orders of magnitude between the implanted and the non-implanted oxide layer) and not to the absolute value of the anode-cathode resistance, which remains high because the resistor is extremely thin ($0.2 \mu\text{m}$). Under operating conditions the measured leakage current is $\approx 100 \text{ pA/cm}^2$. A low leakage current is, obviously, an advantage for low noise and power dissipation.

2.3 The readout structure

Because the back plane is only an induction (not amplifying) plane, the choice of the electrode structure it is almost free in shape (X, Y, r, ϕ , pad, pixel, small angle stereo, etc.) and sampling pitch (down to $50 \mu\text{m}$). In the present work a pad structure is described. It

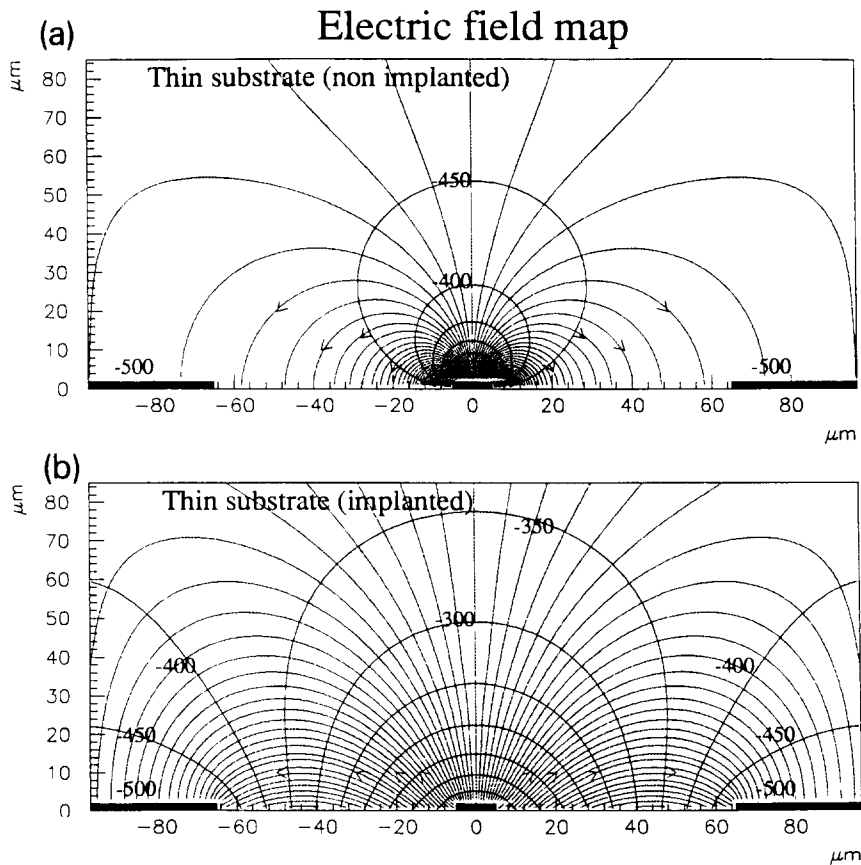


Fig. 3 (a) Field and equipotential lines for a not implanted thin substrate. (b) The same as (a), but for an implanted thin substrate.

consists of a 16×8 matrix of 0.8 cm^2 pads. To reduce the parasitic capacitance toward the low resistivity substrate and toward the side cathode strips, the pad is designed to be almost metal empty, i.e. the metal has been etched away everywhere excluding a thin ($50 \text{ }\mu\text{m}$ wide) strip running parallel with the anode strip and just behind it. This strip, which is only $2 \text{ }\mu\text{m}$ below the anode strip, will collect a large fraction of the induction signal. Sixty of these short strips (6 mm long) are then connected to each other by a $10 \text{ }\mu\text{m}$ wide strip to form the pad (see fig. 6). If minimum pad capacitance is needed, it would be better to increase the thickness of the thermal oxide layer to, for example, $10 \text{ }\mu\text{m}$ which is technically feasible or to build the same device, instead of on low resistivity silicon, on a good insulator like a $200 \text{ }\mu\text{m}$ thick quartz wafer. Table 1 shows the capacitance matrix of the MSGC electrodes for a thickness of 2, 10, and $200 \text{ }\mu\text{m}$ of the oxide layer below Metal 1 (the thickness of the PECVD oxide below Metal 2 being fixed at $2 \text{ }\mu\text{m}$). The diagonal elements of this matrix represent the total capacitance to ground of the various electrodes, while the off-diag-

onal elements represent the partial capacitance of each electrode with respect to the others. In our geometry, the overall pad capacitance would be 480, 230, and 100 pF for, respectively, 2, 10, and $200 \text{ }\mu\text{m}$ substrate thickness. It is also interesting to observe that the anode capacitance, in spite of its close proximity to the back electrode, remains rather low ($\approx 2 \text{ pF/cm}$).

The readout structure presented in this paper could provide a high resolution measurement ($\approx 30 \text{ }\mu\text{m}$ rms) of the coordinate orthogonal to the anode strips (ϕ projection, for example), plus a coarser measurement ($\approx 1.7 \text{ mm}$ rms) of the coordinate along the strip (z projection) together with a powerful identification of which part of the detector has been hit exploiting the internal subdivision in 128 smaller elements (the pads). This electrode geometry is particularly useful to resolve the large particle multiplicity expected at the new hadron colliders.

In the HV bias scheme we adopted the anodes are kept at the virtual ground of the readout amplifiers while the back and side cathodes are connected to a common negative potential through individual $1 \text{ M}\Omega$

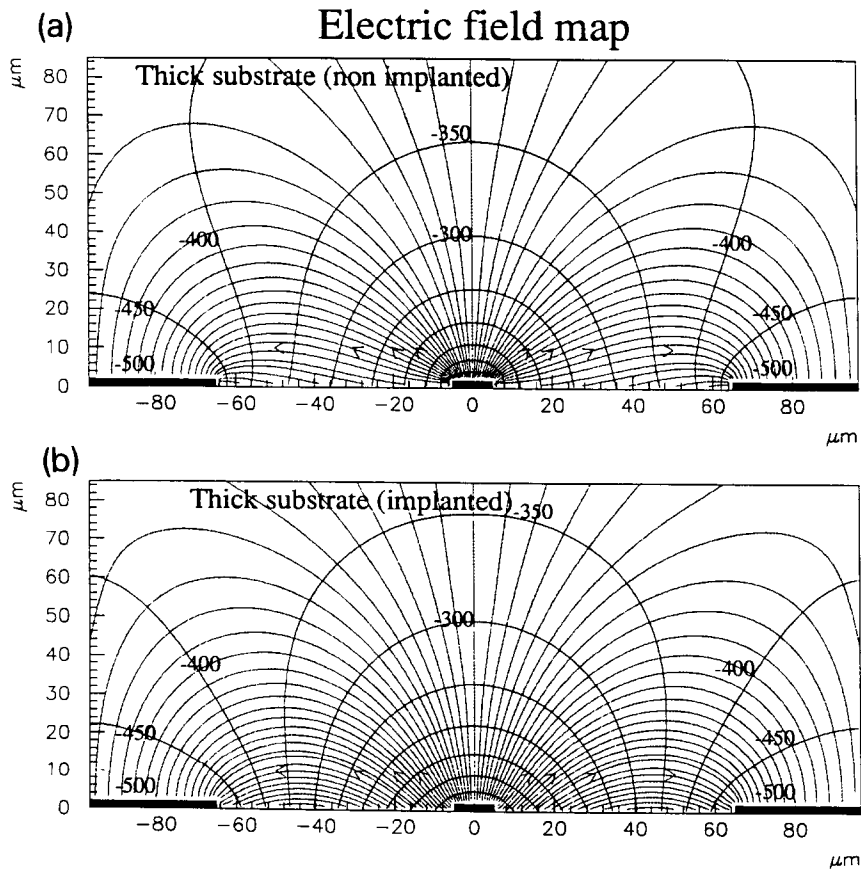


Fig. 4. (a) Field and equipotential lines for a not implanted thick substrate. (b) The same as (a), but for an implanted thick substrate.

polysilicon resistors directly fabricated on the detector. Because no fast signal is available on the side cathode strips (which are electrically shielded by the much closer back plane) we can connect these electrodes to high voltage through individual current limiting resistors without the risk of significant cross-talk, avoiding also the need of bulky HV blocking capacitors. With this setup the detector can be thought of as an array of 512 fully independent, HV decoupled, detection elements. This is a very safe condition to avoid or reduce damage to the strips in case of sparking.

A microphotograph of a detail of the detector internal structure (the bias scheme) is shown in fig. 7.

3. The detector characteristics

3.1. The signals and the gain

Fig. 8 shows the signals obtained from one anode strip when the detector was illuminated with the Cu

K_{α} line produced by an X-ray tube. Because the range of the 8 keV photoelectron in the Ar(95%)-DME (5%) filling gas mixture is rather large ($> 300 \mu\text{m}$) compared with the anode pitch, the pulse height distribution is almost continuous (no photopeak or energy resolution can be observed from a single strip). One should note the fast peaking time of the signals (20 ns). Fig. 9 shows the signal from one anode strip which is triggering the signal from the corresponding pad hit when the 8 keV X-ray beam was collimated to a 2 mm^2 spot. Because the pad collects the full charge from the photon conversion, the pad signal has a well defined photopeak showing the characteristic good proportionality of this class of detectors. The large pad capacitance affects strongly the signal/noise ratio, which is, obviously, much worse for the pad than for the anode strip. Furthermore, the RC product of the pad parallel capacitance and of its series resistance ($\approx 200 \Omega$) slows down the transfer of the charge collected by the pick-up electrode to the input capacitance of the fast amplifier. Because of this ballistic deficit the pad signal appears

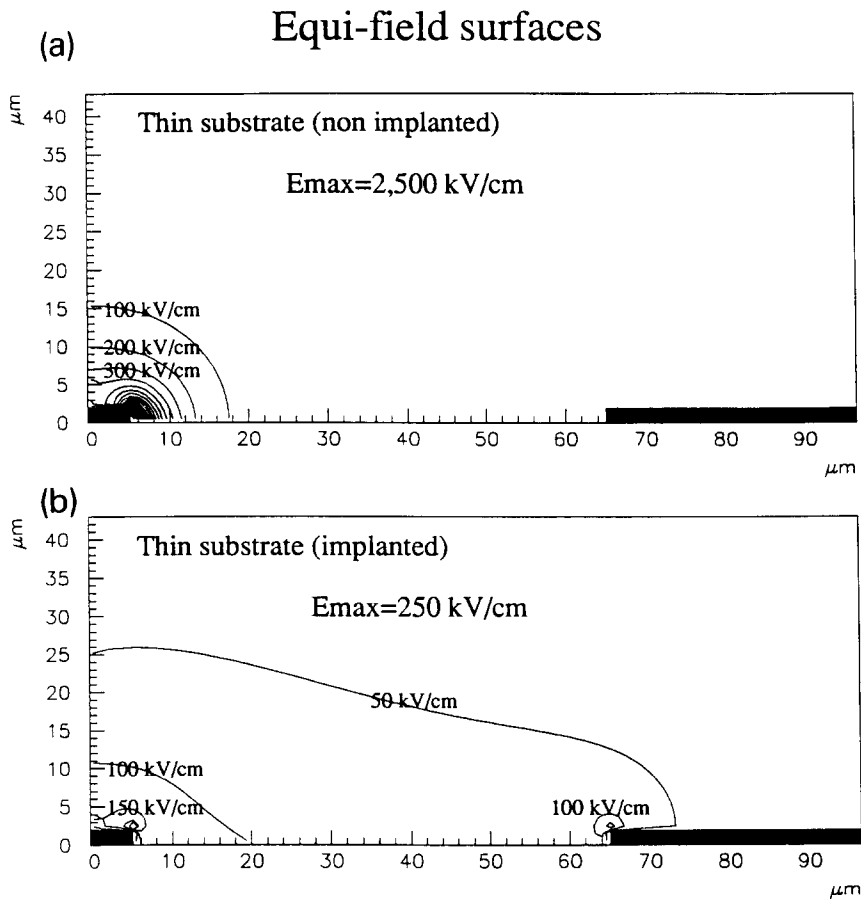


Fig. 5. (a) Equifield lines for a not implanted thin substrate. (b) The same as (a), but for an implanted thin substrate.

slower and smaller than the anode signal. The use of thicker oxide or of an insulating substrate will substantially improve on both aspects. A detector identical to

the one presented here but built on a 200 μm thick quartz wafer is under construction in our laboratory.

The dependence of the pulse amplitude on the

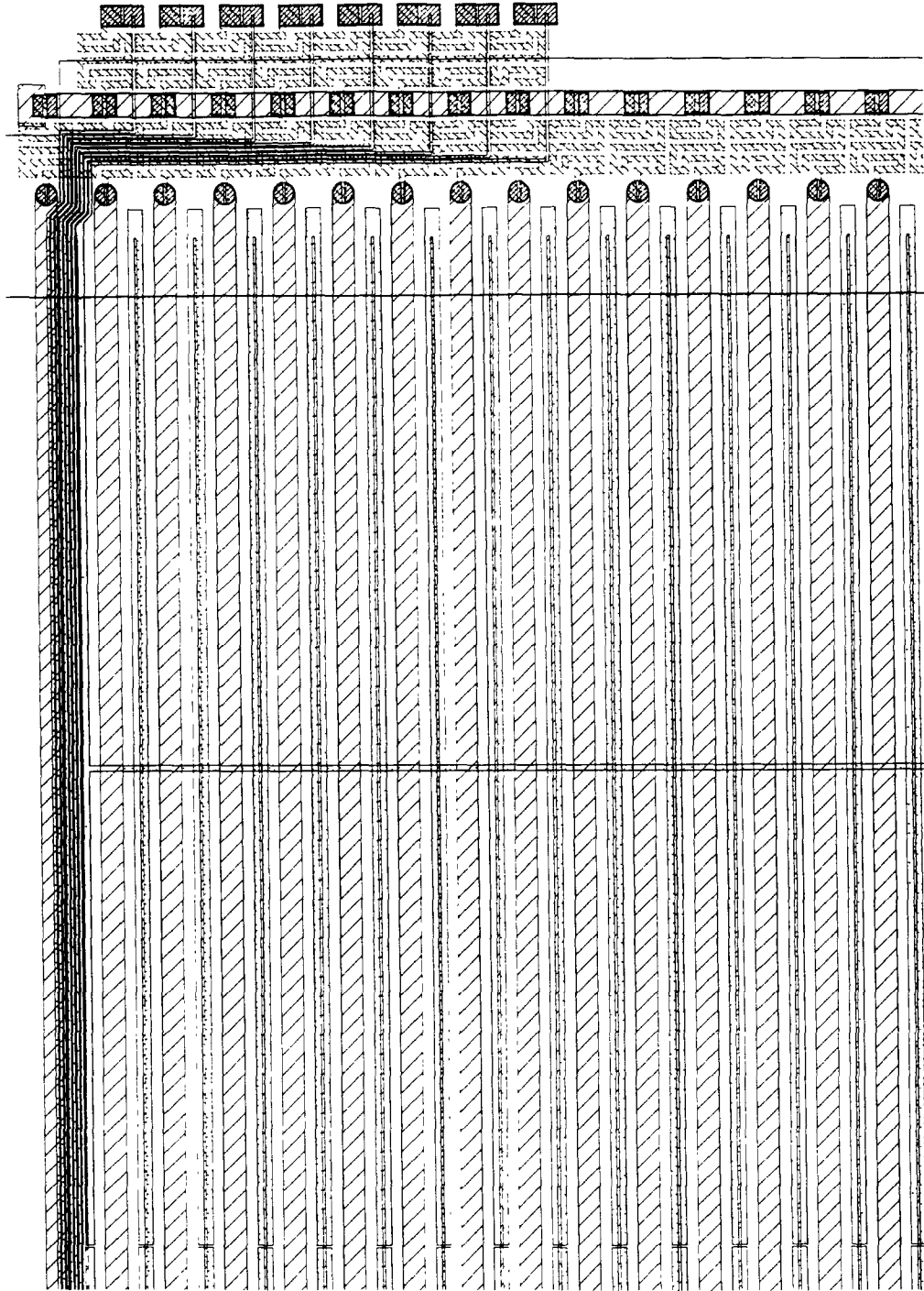


Fig. 6 Schematics of the MSGC electrode geometry.

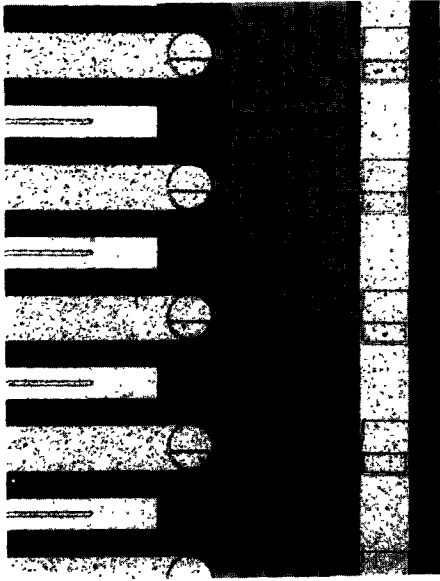


Fig. 7. A microphotograph of a detail of the detector internal structure (the bias scheme).

cathode voltage is reported in fig. 10. At 360 V the gas gain has been measured to be $\approx 5 \times 10^3$. As already observed in detectors of similar design, this anode-cathode potential difference is somewhat lower and therefore safer than the one needed for detectors whose anode strips lie directly on a thick ($> 100 \mu\text{m}$) insulating substrate.

The general performance of this detector in terms of rate capability and energy resolution is very similar to that measured by us [12] in previous detectors based on the same principle and therefore are not reported here.

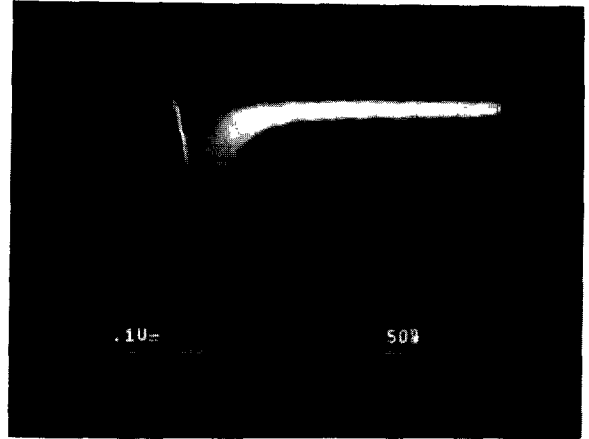


Fig. 8. The signal obtained from one anode strip with 8 keV photons.

3.2. Charging-up

A crucial point connected with the kind of insulating substrate adopted, in our case represented by the implanted SiO_2 layer, is the so-called charging-up effect [14,15], namely a time and flux dependent modification of the gain due to the charging-up of substrate surface. To study this problem two kinds of measurement have been performed. The first is a very short-term measurement (on a time scale of seconds) of the signal current as a function of time at different photon fluxes (i.e. at different X-ray tube currents). For this measurement we have used a detector which had not been irradiated before. Fig. 11 shows the signal current (which is supposed to be proportional to the gas gain)

Table 1
The MSGC capacitance matrix for three values of the thickness of the insulator below Metal 1

	Substrate	Pad	Side cathode	Anode
Oxide thickness: 2 μm				
Substrate		1200 pF/cm ²	490 pF/cm ²	13 pF/cm
Pad			600 pF/cm ²	0.71 pF/cm ²
Side cathode				13 pF/cm
Anode				2.1 pF/cm
Oxide thickness: 10 μm				
Substrate		280 pF/cm ²	120 pF/cm ²	3.1 pF/cm
Pad			220 pF/cm ²	1.3 pF/cm ²
Side cathode				3.1 pF/cm
Anode				2.1 pF/cm
Oxide thickness: 200 μm				
Substrate		0.035 pF/cm ²	13 pF/cm ²	0.33 pF/cm
Pad			130 pF/cm ²	12 pF/cm ²
Side cathode				0.61 pF/cm
Anode				2.1 pF/cm

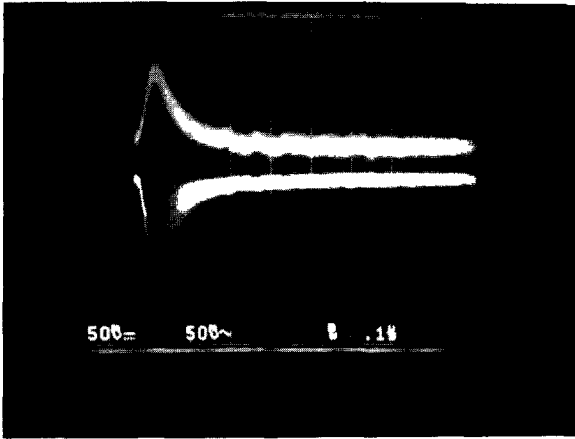


Fig. 9. The signal obtained from one anode strip (lower trace) triggering the signal from the corresponding pad (upper trace).

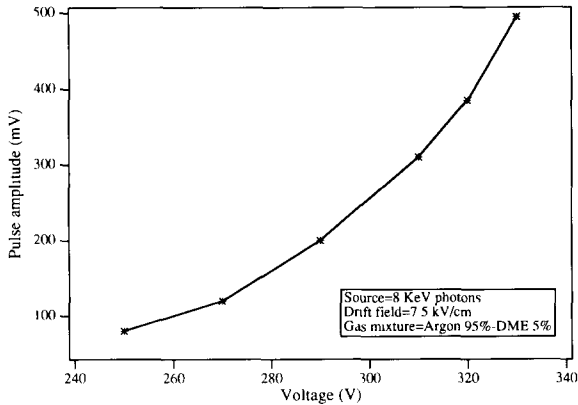


Fig. 10. Dependence of the pulse amplitude on the cathode voltage.

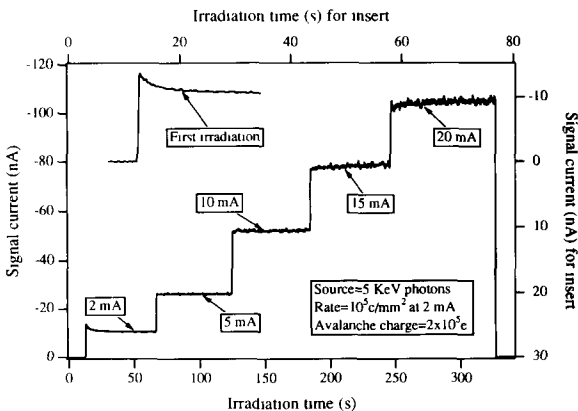


Fig. 11. The signal current as a function of time at different photon fluxes for a detector never irradiated before.

as recorded with a Keitley 487 picoammeter at different tube current settings (from 2 to 20 mA, corresponding roughly to a flux between 10^5 and 10^6 photons/mm² s). The sampling frequency was 10 Hz. Only during the first few seconds of the first irradiation it was possible to observe a reduction ($\approx 25\%$) of the current. During all the following irradiations the gain was very stable. The most interesting feature of this measurement is the observation that the gain plateau does not depend on the flux (i.e. it is the same at any flux). The flux level affects only the time it takes to reach the plateau. This flux independence is shown in fig. 12 which reports the normalized signal current as a function of time for several X-ray tube current settings. Before dividing the signal current by the tube current we checked the linearity between tube current and flux (see fig. 13). This check was performed at low rate by suitably filtering the tube output. The fast reduction of gain during the first irradiation is local and it is not recoverable (at least in a short time). This is demonstrated in fig. 14 which shows three records of the signal current taken at a time interval of 8 and 48 hours in the same point previously irradiated for a few minutes. Between the first and second measurement the HV was left on, while between the second and third measurement it was switched off. The three records are almost identical.

The second charging-up measurement was a study of the long-term stability (on a time scale of several hours) of the gas gain. For this purpose the mean signal amplitude as recorded by a Tektronix 2440 digital oscilloscope was monitored over a period of more than 12 hours of continuous running at an X-ray flux of 10^5 particles/mm² s (see fig. 15). This flux is more than one order of magnitude higher than what is expected at LHC at 50 cm from the beam axis. No significant gain variation was observed.

The conclusion from the combination of these measurements is that charging, at least in the standard meaning of flux dependent change of gain due to the accumulation of positive ions on the substrate, is not a serious problem for this detector. This is also a confirmation that the implantation of the oxide is an effective technique to provide long-term stable operation of the device [3].

3.3. Ageing

An important factor which has to be taken into account when considering possible applications of these detectors at high luminosity colliders is the ageing effect, i.e. the deterioration of the detector response when continuously exposed (on a time scale of several years) to a high flux of charged particles [14]. To address this point an accelerated study has been performed in the laboratory with a very simple gas system

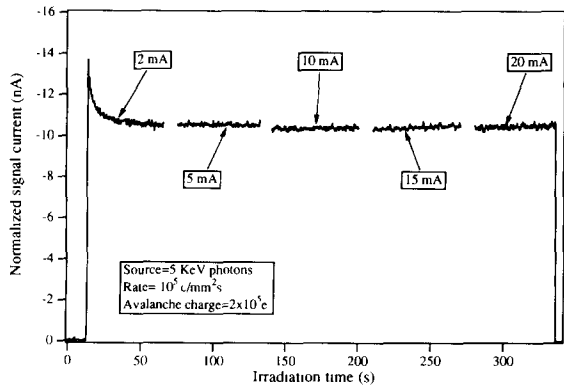


Fig. 12. The normalized signal current as a function of time at different photon fluxes.

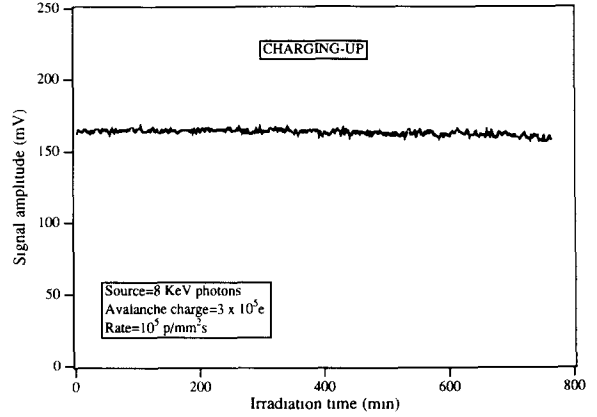


Fig. 15. Long-term measurement of the gain stability.

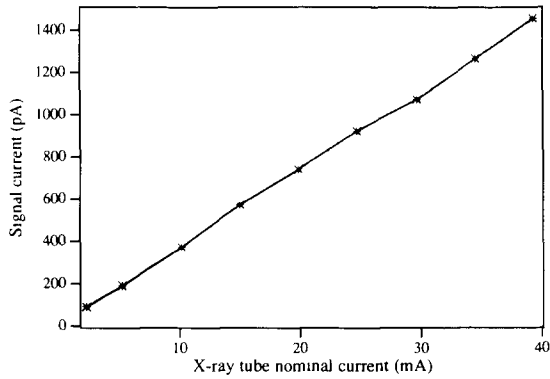


Fig. 13. The linearity curve between nominal tube current and output photon flux.

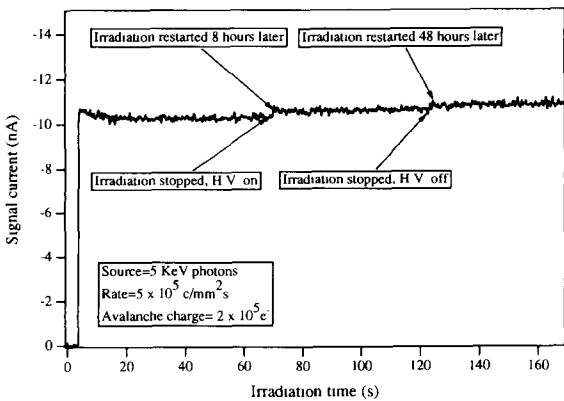


Fig. 14. The signal current as a function of time taken at different time intervals.

based on the standard, CERN type, gas mixer, nylon tubing and brass pressure regulator. Argon was of research grade (99.9995%) while the purity of DME, supplied by Union Carbide (Belgium) was not known. A reduction of 20% in the average value of the signal amplitude, together with some degradation of the energy resolution, has been observed (see fig. 16) after the exposure to a flux of $\approx 2 \times 10^6$ particles/cm s for a period of four days. With an avalanche charge of 4×10^5 electrons this corresponds to an integrated charge of more than 40×10^{-3} C/cm on the anode strip. The observed gain fluctuations are primarily due to pressure and temperature changes in the laboratory during the measurement. This integrated flux is equivalent to more than eight years of running at the design luminosity of LHC [16] at 50 cm from the beam axis, including the effect of a 4 T magnetic field. The gain reduction is not recoverable and is a local effect. We have observed a lack of recovery of the initial gain when the irradiation was stopped for 10 hours and

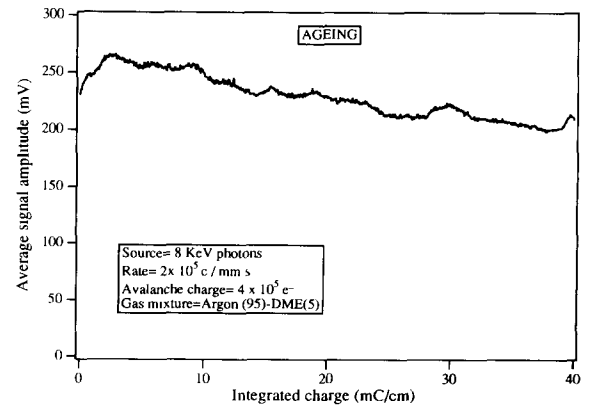


Fig. 16. Very long-term measurement of the gain stability (ageing).

then restarted at the same point, while recovery of the full initial gain was observed when the beam spot was moved a few mm along the same strips, just outside the previously irradiated area. At the irradiated point the recovery of the original gain was obtained with ≈ 10 V increase of the anode-cathode potential difference.

It is interesting to observe that a similar level of radiation resistance was already achieved by the detectors used in the NA12 experiment at CERN. These one dimensional MSGCs have been exposed to a peak flux of $\approx 10^6$ particles/mm² s during a 100 days physics run in the 1992 summer. The global duty cycle was of the order of 10%.

4. Conclusions

The thin, large area MSGC presented in this paper has been designed primarily with the idea of using it as a building block of a large tracking system at LHC/SSC.

For this reason the readout has been organized as one high resolution projection (ϕ , for example) plus macroscopic pixels to solve ambiguities and to provide true space points. Its charging-up and ageing properties have been measured under realistic conditions and they show that these detectors will survive for at least eight years of operation at the design luminosity of LHC.

Finally, it is worth mentioning that this large area detector with simple modifications of the readout organization could also find many interesting applications in different fields, such as astrophysics, synchrotron

radiation and medical physics as an X-ray imaging device.

Acknowledgements

We thank G. Decarolis, M. Favati and C. Magazzu' of INFN-Pisa for their enthusiastic technical support.

References

- [1] A. Oed, Nucl. Instr. and Meth. A 263 (1988) 351.
- [2] F. Angelini et al., Nucl. Instr. and Meth. A 283 (1989) 755.
- [3] F. Angelini et al., Particle World 1 (3) (1990) 85.
- [4] M.H.J. Gijsberts et al., Nucl. Instr. and Meth. A 313 (1992) 377.
- [5] F. Angelini et al., Nucl. Instr. and Meth. A 315(1992) 21.
- [6] RD22 Collaboration, CERN/DRDC 92-51.
- [7] CMS Collaboration, Letter of Intent, CERN/LHCC 92-3; ATLAS Collaboration, Letter of Intent, CERN/LHCC 92-4; L3P Collaboration, Letter of Intent, CERN/LHCC 92-5.
- [8] SDC Collaboration, Technical design report, SSCL-SR-1215.
- [9] F. Angelini et al., Nucl. Instr. and Meth. A 314 (1992) 450.
- [10] S.F. Biagi et al., Nucl. Instr. and Meth. A 323 (1992) 258.
- [11] T. Nagae et al., Nucl. Instr. and Meth. A 323 (1992) 258.
- [12] F. Angelini et al., Nucl. Instr. and Meth. A 323 (1992) 229.
- [13] J.J. Florent et al., CERN-PPE/92-78.
- [14] R. Bouclier et al., CERN-PPE/93-04.
- [15] J.E. Bateman and J.F. Connolly, RAL-92-085.
- [16] T. Meyer, Proc. ECFA LHC Workshop, CERN 90-10, Vol. 3 (1990) p. 208.